

CO₂ Reduction

How to cite:

International Edition: doi.org/10.1002/anie.202001953

German Edition: doi.org/10.1002/ange.202001953

2-Aminobenzenethiol-Functionalized Silver-Decorated Nanoporous Silicon Photoelectrodes for Selective CO₂ Reduction

Miao Kan, Zhifei Wang Yan, Xingtao Wang, Jeremy L. Hitt, Langqiu Xiao, Jeffrey M. McNeill, Yong Wang, Yixin Zhao,* and Thomas E. Mallouk*

Abstract: A molecularly thin layer of 2-aminobenzenethiol (2-ABT) was adsorbed onto nanoporous p-type silicon (b-Si) photocathodes decorated with Ag nanoparticles (Ag NPs). The addition of 2-ABT alters the balance of the CO₂ reduction and hydrogen evolution reactions, resulting in more selective and efficient reduction of CO₂ to CO. The 2-ABT adsorbate layer was characterized by Fourier transform infrared (FTIR) spectroscopy and modeled by density functional theory calculations. Ex situ X-ray photoelectron spectroscopy (XPS) of the 2-ABT modified electrodes suggests that surface Ag atoms are in the +1 oxidation state and coordinated to 2-ABT via Ag–S bonds. Under visible light illumination, the onset potential for CO₂ reduction was –50 mV vs. RHE, an anodic shift of about 150 mV relative to a sample without 2-ABT. The adsorption of 2-ABT lowers the overpotentials for both CO₂ reduction and hydrogen evolution. A comparison of electrodes functionalized with different aromatic thiols and amines suggests that the primary role of the thiol group in 2-ABT is to anchor the NH₂ group near the Ag surface, where it serves to bind CO₂ and also to assist in proton transfer.

Introduction

Current global trends in energy use and its impact on climate have created a pressing need for a carbon-neutral cycle of storage and use of renewable energy.^[1,2] Because of the high energy density of carbon-based fuels and the well-developed infrastructure for their transportation, storage, and use, the conversion of gaseous carbon dioxide to fuel feedstocks has attracted widespread attention.^[3–6] One of the impediments to the efficient use of sunlight or renewable electrical energy to electrolyze CO₂ is the high overpotential needed to drive its reduction to the one-electron intermediate, 'CO₂^{•-}. The overpotential can be lowered by supplying

protons to the catalytic center through a sequential electron-proton transfer or proton-coupled electron transfer (PCET) process.^[5] A second challenge for electrolysis in protic media is the hydrogen evolution reaction, which occurs in competition with CO₂ reduction.^[6,7] Many different heterogeneous electrocatalysts have been studied for CO₂ electrolysis, and the most effective are Ag, Au, and Pd for reduction to C₁ products (CO and formate), and Cu and its alloys for reduction to C–C bonded molecules.^[8–12] With Ag, the main products are CO and H₂, but the potential range for reduction to CO with high Faradaic efficiency is narrow, and this limits the practical current densities that can be achieved.^[13–15]

An alternative to a photovoltaic-electrolyzer system is the direct reduction of CO₂ at the surface of an illuminated semiconductor photoelectrode.^[16,17] As early as 1978, Hallmann demonstrated the photoreduction of CO₂ at p-GaP electrodes.^[18] Subsequently other semiconductors including TiO₂, InP, GaP, ZnO, CdS, Si, and WO₃ were studied as components of photoelectrochemical and photocatalytic CO₂ reduction systems.^[19–22] Among these semiconductors, p-type silicon with band gap of 1.1 eV is of special interest because of its nearly ideal band gap for tandem absorber systems and the falling cost as well as increasing efficiency of silicon photovoltaics.^[23–25] The Faradaic efficiency of direct CO₂ reduction at p-Si was shown to be high when carried out in non-aqueous electrolytes or at high pressure.^[26,27] To further improve the CO₂ reduction efficiency, cocatalysts such as reduced graphene oxide,^[28,29] Sn nanorods,^[30] silver nanowires,^[31] and gold mesh^[32] have been combined with the semiconductor. For Ag-catalyzed CO₂ reduction, CO is regarded as a key target compound because of its favorable economics as a building block of chemicals and fuels.^[33] But the partial current density of C₁ products under solar illumination at p-Si is still limited to about 7 mA cm⁻², even with reagents added to inhibit hydrogen evolution, because of the kinetically slow CO₂ reduction process.^[34–36] Nanostructuring p-Si electrodes can improve light absorption and also provide a higher surface area for electrocatalysis. However black silicon (b-Si), produced by etching planar Si to increase the surface area and catalyzed with metals such as Ag, promotes H₂ generation and therefore lowers the Faradaic efficiency for CO₂ reduction.

Herein, we investigate the functionalization of b-Si/Ag with 2-aminobenzenethiol (2-ABT) and related molecules for CO₂ reduction. 2-ABT was adsorbed onto the surface of Ag nanoparticles forming a molecularly thin layer. The adsorption of 2-ABT results in oxidation of surface Ag atoms, which act as the active catalyst for CO₂ reduction. The Faradaic efficiency for CO₂ reduction to CO was increased from 50 %

[*] M. Kan, X. T. Wang, Dr. Y. Wang, Prof. Y. X. Zhao
School of Environmental Science and Engineering, Frontiers Science Center for Transformative Molecules, Shanghai Jiao Tong University Shanghai 200240 (China)
E-mail: yixin.zhao@sjtu.edu.cn

M. Kan, Z. F. W. Yan, J. L. Hitt, L. Q. Xiao, J. M. McNeill,
Prof. T. E. Mallouk
Department of Chemistry
University of Pennsylvania
Philadelphia, PA 19104 (USA)
E-mail: mallouk@sas.upenn.edu

Supporting information and the ORCID identification number(s) for the author(s) of this article can be found under:
<https://doi.org/10.1002/anie.202001953>.

to 75 %, most likely because 2-ABT assists in shuttling CO_2 and H^+ to the catalytic Ag surface. Interestingly, this effect is not observed with the *para*-isomer 4-ABT, suggesting that the proximity of the $-\text{NH}_2$ group to the surface is important in enhancing the catalytic reduction of CO_2 to CO .

Results and Discussion

Electrode Fabrication

Planar p-type Si (p-Si, E0) and nanoporous p-type Si (b-Si, E3) electrodes were prepared by an Ag-assisted electroless etching process and then modified with Ag nanoparticles and/or with 2-ABT according to the scheme shown in Figure 1. The 2-aminobenzenethiol (2-ABT) molecule is relatively insoluble and stable in neutral aqueous solution.^[37–39] This molecule does not adsorb significantly on unmodified Si electrodes (E1), as evidenced by the lack of observable adsorbate peaks in the FTIR spectrum (Figure S1 in the Supporting Information), but is expected to bond strongly to Ag-modified Si because of the well-documented affinity of thiols for noble metal surfaces.^[40] Silver nanoparticles (Ag NPs) were electrolessly deposited on planar and b-Si to form Si/Ag (E2') and b-Si/Ag (E4), respectively. The amount and size of the Ag NPs could be controlled by the deposition time (60 s in most cases). According to SEM images shown in Figure S2 and Table S1, Ag particles cover about half of the porous silicon surface. Modeling the silver nanoparticles as hemispheres, their surface area can be calculated as roughly twice that of the porous silicon substrate. After immersion in 2-ABT/methanol solution for 5 min and rinsing with methanol, b-Si/Ag/2-ABT (E5) electrodes were obtained. The amount of 2-ABT initially deposited was in the range of several nmol cm^{-2} , based on a linear calibration curve of two peaks (at 300 nm and 1030 nm) in the UV/Vis-NIR transmission spectra, as shown in Figure S3. Before rinsing, micron-size patches of residual 2-ABT were apparent (Figure S4). Further careful rinse with methanol gave b-Si/Ag/2-ABT photoelectrodes. UV/Vis spectra (Figure S5) indicated a 2-ABT coverage of around 16 nmol cm^{-2} based on the geometric area of Si, or approximately 0.3 nmol cm^{-2} of 2-ABT relative to the surface area of Ag, which is in the range of

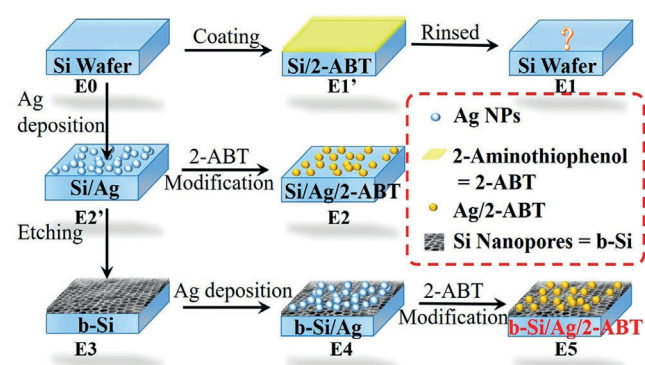


Figure 1. Surface modification process for Si photoelectrodes.

monolayer coverage. The low absorbance of the 2-ABT adsorbate layer between 300 and 1030 nm indicates that at this loading, 2-ABT does not interfere with the transmission of excitation light to the b-Si electrode.

Characterization

The micro-scale structure of a b-Si/Ag/2-ABT electrode (E5) is shown in scanning electron microscopy (SEM) images in Figure 2. Images of b-Si (E3 in Figure 2 a) and b-Si/Ag (E4 in Figure 2 b) are shown for comparison. Freshly etched b-Si has vertical nanopores with diameters ranging from 10 to 100 nm and a depth of about 500 nm (Figure 2 d), resulting in an around 25 times higher surface area than that of p-Si. Based on the SEM images, no Ag nanoparticles are discernable on the b-Si surface, but the rough edges of the pores, which are evident on the top surface, may provide the most active sites for secondary Ag deposition.^[23,24] Figure 2 b shows the distribution of Ag nanoparticles (Ag NPs) on the top surface of b-Si/Ag. Ag NPs with diameters less than 50 nm are distributed at the pore edges and on top of the Si surface. While some Ag nanoparticles can also enter the pores, this could not be directly confirmed from secondary-electron-imaging (SEI) cross-sectional images in Figure 2 d due to the similar sizes of the nanopores and the Ag nanoparticles.^[41,42] No change in the Ag nanoparticle morphology was apparent when 2-ABT was adsorbed to make b-Si/Ag/2-ABT (E5 in Figure 2 c and f) after methanol rinsing, indicating that the adsorbed layer is too thin to be observed by SEI-SEM.

To further explore the distribution of Ag and 2-ABT, other physicochemical methods were applied. Ag nanoparticles with a range of diameters could be qualitatively distinguished by the back-scattered-electron-imaging (BSE) SEM, which provides contrast according to the atomic mass of particles but with lower spatial resolution as shown in

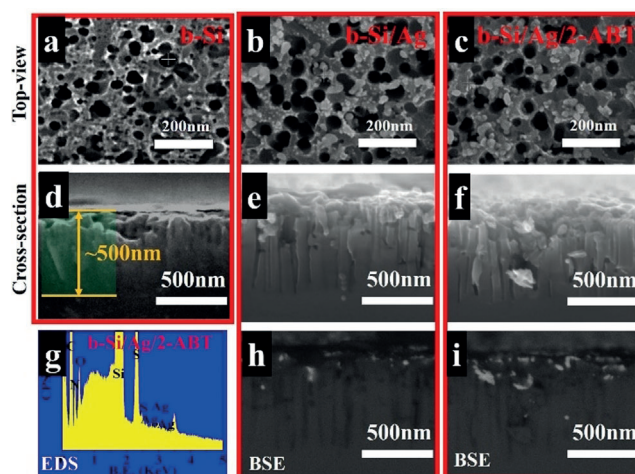


Figure 2. Top-view SEI-SEM images, cross-sectional-view SEI-SEM images and BSE-SEM images of b-Si (E3), b-Si/Ag (E4), and b-Si/Ag/2-ABT (E5) and an energy-dispersive X-ray spectrum (g) of b-Si/Ag/2-ABT. a), d) for b-Si; b), e), h) for b-Si/Ag; and c), f), i), g) for b-Si/Ag/2-ABT.

Figure 2h,i. The diameters of the Ag nanoparticles that appeared in these images were approximately 50 nm, which is consistent with the diameters of those on top. Energy-dispersive X-ray spectroscopy (EDS) in the SEM system was used to confirm the adsorption of 2-ABT molecules by monitoring the appearance of Ag, N and S signals, as shown in Figure 2g. The apparent content of elemental Ag was very low (0.3 atom %) and close to the value found for b-Si/Ag in Figure S6. While EDS analysis is not quantitative and is complicated by the porous structure of the electrode, it provides clear evidence for the presence of N and S in the b-Si/Ag/2-ABT samples, as shown in Figure 2g; in contrast, no N or S signal was detectable with b-Si/Ag (Figure S6). Although the surface is porous (Figure 2c), all elements appear evenly distributed as shown in Figure S7, confirming that both Ag and 2-ABT reside in the pores of the electrode.

More morphological details could be obtained with scraps from the surface of the Si/Ag/2-ABT electrodes by transmission electron microscopy (TEM), as shown in Figure 3. The bright-field (BF) TEM image in Figure 3a shows an arched surface on a scale of several hundred nanometers in b-Si/Ag/2-ABT, confirming that Ag enters the pores. The bright spots with diameters ranging from 10 to 100 nanometers in the High-Angle-Annular-Dark-Field (HAADF) TEM image (Figure 3b) result from elements of high atomic mass, that is, Ag. EDS elemental mapping of Si, Ag, N, S is shown in Figure 3c–f. Dense Si is distributed at the bottom of the structure (Figure 3c), whereas Ag nucleates on the surface of Si and grows into larger particles (up to 100 nm in Figure 3b,d). Note that the elemental distribution of S and N from 2-ABT is coincident with that of Ag, but not with that of Si. The core-shell structure of Ag-ABT in Si/Ag/2-ABT

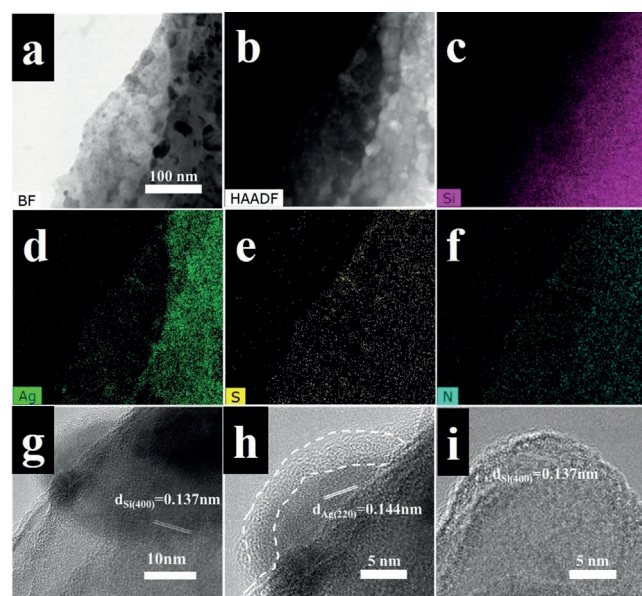


Figure 3. Transmission electron microscopy (TEM) analysis of b-Si/Ag/2-ABT. Low-magnification images: a) BF-STEM, b) HAADF-STEM images; Relative EDS mapping of c) Si, d) Ag, e) S, and f) N; High-resolution TEM images: g) Si/Ag/2-ABT at 10 nm scale, h) Magnified image, showing an approximately 3 nm thick amorphous layer (indicated by the broken line) of Ag and 2-ABT; i) Si without Ag.

electrodes was confirmed by high-resolution TEM (HRTEM), as shown in Figure 3g,h. No amorphous layer was evident on the surface of unmodified Si as shown in Figure 3i, whereas an Ag nanoparticle identified by its (220) lattice fringes with an amorphous overlayer of approximately 3 nm thickness could be distinguished the Si substrate with (400) lattice fringes. A clearer image with an Ag facet (111) on Si (400) is shown in Figure S8. The core-shell structure could also be imaged with 500 nm Ag NPs, in which Ag was covered by an amorphous layer, only around 3 nm of which remained adsorbed to the Ag surface after rinsing as shown in Figure S9 and S10. These images are consistent with a strong covalent interaction between Ag and 2-ABT but a weak interaction between Si and 2-ABT, in agreement with the IR data in Figure S1.

The surface modification of b-Si/Ag/2-ABT was further confirmed by FTIR as shown in Figure 4. Since b-Si/Ag itself has a complicated IR spectral background, spectra of pl-Si samples were first recorded for comparison purposes. Spectra were background corrected by subtracting the relevant reference spectrum, which is denoted in Figures as (background). Strong peaks that can be attributed to 2-ABT with pl-Si/Ag/2-ABT (pl-Si/Ag) (E1, which contains a thick drop-cast 2-ABT layer) appear at 1303 cm^{-1} for C–C or C–N stretching, 1248 cm^{-1} for C–C stretching, and 1446 and 1472 cm^{-1} for C=C stretching (Figure S11a and S11b).^[43,44] These spectral features were not observed with methanol-rinsed pl-Si (E1) or pl-Si/Ag (E2'), indicating that they come from the phenyl groups of 2-ABT. Much weaker peaks, presumably from the molecularly thin 2-ABT layer, appear in the spectra of b-Si/Ag/2-ABT. In the spectrum of 2-ABT, peaks at 1584 and 1622 cm^{-1} are typical of NH_2 scissor and C–N stretching modes, respectively, whereas only weak peaks at around 1610 cm^{-1} appear in the b-Si/Ag/2-ABT spectrum. Also, the peak near 2600 cm^{-1} corresponding to S–H bonding in 2-ABT is not observed in the spectrum of pl-Si/Ag/2-ABT in Figure S11c and S11d.^[45] Comparing the FTIR baseline spectrum of b-Si/Ag with spectra of pl-Si/Ag/2-ABT and b-Si/

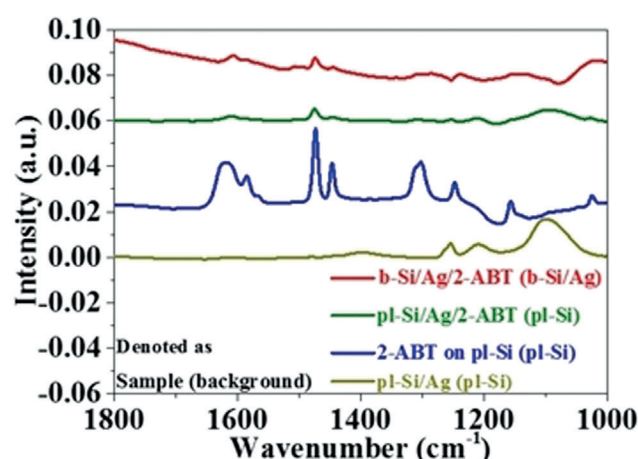


Figure 4. Background-corrected FTIR spectra ($1800\text{--}1000\text{ cm}^{-1}$) of pl-Si/Ag (pl-Si), 2-ABT on pl-Si (pl-Si) before rinsing, pl-Si/Ag/2-ABT (pl-Si), and b-Si/Ag/2-ABT (b-Si/Ag). Background sample for each trace is denoted as (background).

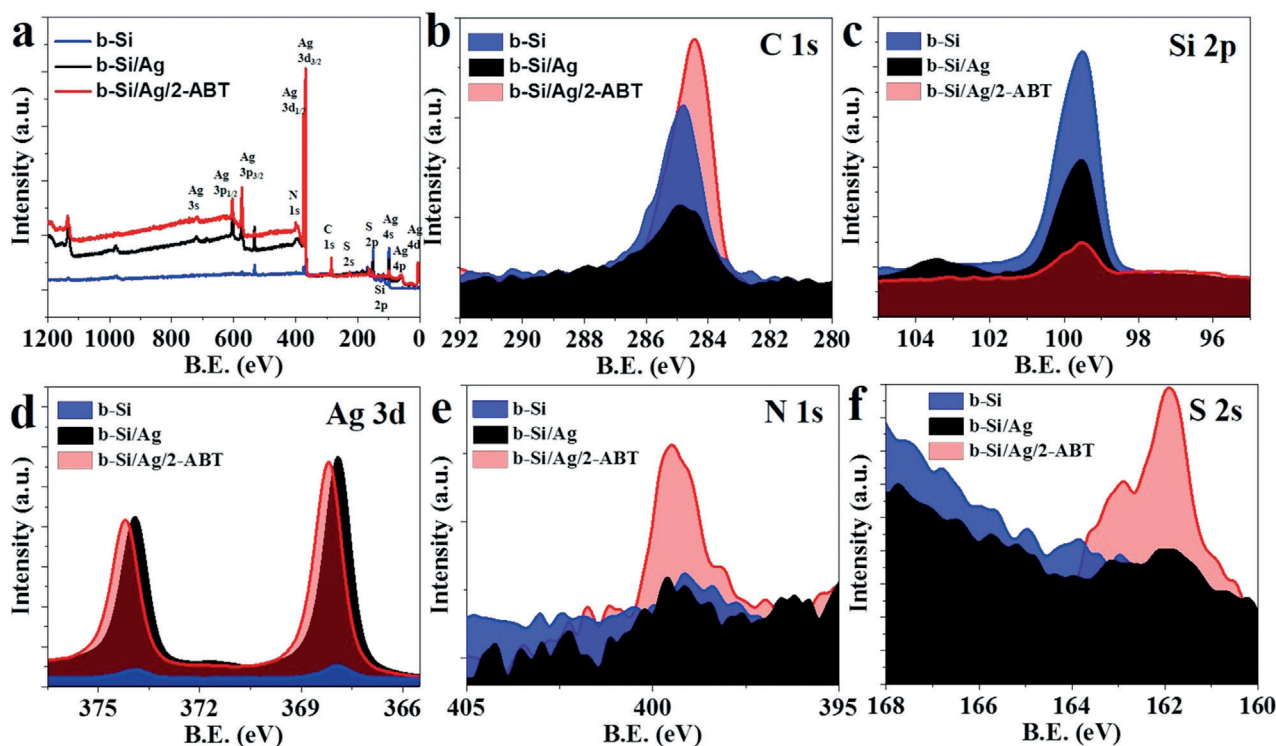


Figure 5. XPS a) survey spectra, and higher resolution spectra in the b) C 1s, c) Si 2p, d) Ag 3d, e) N 1s, and f) S 2p regions.

Ag/2-ABT (Figure 4), peaks at 1446 cm^{-1} , 1472 cm^{-1} , and 1610 cm^{-1} are present in the spectra of both 2-ABT-containing samples, consistent with adsorption of an ultrathin layer of 2-ABT on Ag.

To better understand the chemical bonding between Ag and 2-ABT, XPS spectra of b-Si, b-Si/Ag, and b-Si/Ag/2-ABT were obtained and are shown in Figure 5. Figure 5a shows XPS survey spectra and contains peaks that can be attributed to Si, Ag, N, S, and C. All peaks were calibrated with Si_{2p} to minimize charging effects (Figure 5b). Higher resolution spectra of the individual elements are shown in Figures 5c–f. In Figure 5c, the main peak for elemental Si is at 99.5 eV and a peak at 103.2 eV can be attributed to SiO_x on the b-Si/Ag surface. This peak is nearly absent on the 2-ABT treated surface, suggesting that the 2-ABT can inhibit the oxidation of Si to some extent. Both b-Si and b-Si/Ag have peaks attributable to Ag at 373.9 and 367.9 eV, but the latter sample shows much higher intensities. This indicates that some residual Ag remains on the surface of b-Si after initial etching, and much more is present on b-Si/Ag. Interestingly, the Ag peaks shift to higher binding energy after 2-ABT adsorption, suggesting surface oxidation to Ag¹⁺.^[45] The obvious peaks for N 1s and S 2p in Figure 5e,f further confirm the presence of S and N on the b-Si/Ag/2-ABT surface, which is consistent with the EDS results. The relative amounts of S and N on a polished graphite/Ag/2-ABT sample were calculated as 1.08:1 (Figure S12), which agrees with the stoichiometric ratio S/N ratio in 2-ABT.

Because Ag exists as nanoparticles on Si surface, the bonding of a 2-ABT monolayer on Ag was simulated by DFT calculations using a single Ag atom and then Ag (110) as

a model surface.^[46,47] A rough DFT optimization was performed using the B3LYP functional with Gaussian. The 3–21G basis set was employed for C, N, H, S, and the SDD basis set was used for the single Ag atom.^[48] The Ag–S bond length was calculated as approximately 0.25 nm which is similar to that in Ag₂S. The Ag–N distance was calculated as approximately 0.23 nm. Based on these parameters, we focused on the surface structure with the catalytically active Ag (110) surface.^[47] Before the CASTEP calculations, the reconstructed Ag(110) surfaces were modeled by supercells (2 × 2) which included three layers of fcc (110) stacked silver atoms. An overlayer of 2-ABT was added with a 18-Å thick vacuum layer.^[49] The use of OTFG norm-conserving pseudopotentials enabled good convergence at an energy cutoff of 300 eV. The Brillouin zone of the (2 × 2) supercell was first sampled by a (1 × 1 × 1) Monkhorst-Pack grid with fine-quality convergence and ultrafine-quality SCF tolerance. The grids were finally enlarged to (3 × 4 × 1) to obtain the optimized structure in Figure S13. The final Ag–S and Ag–N distances were about 2.5 Å, indicating a chemical interaction between Ag and 2-ABT.

Photoelectrochemistry

The b-Si/Ag/2-ABT photocathodes show significantly enhanced photoelectrochemical performance over unmodified electrodes in a CO₂ saturated 0.2M KHCO₃ solution (pH 6.89) (Figure 6). Linear sweep voltammetry curves (LSVs) were measured in visible light (ca. 66 mW cm⁻²) provided by white light illumination with a 420 nm cutoff

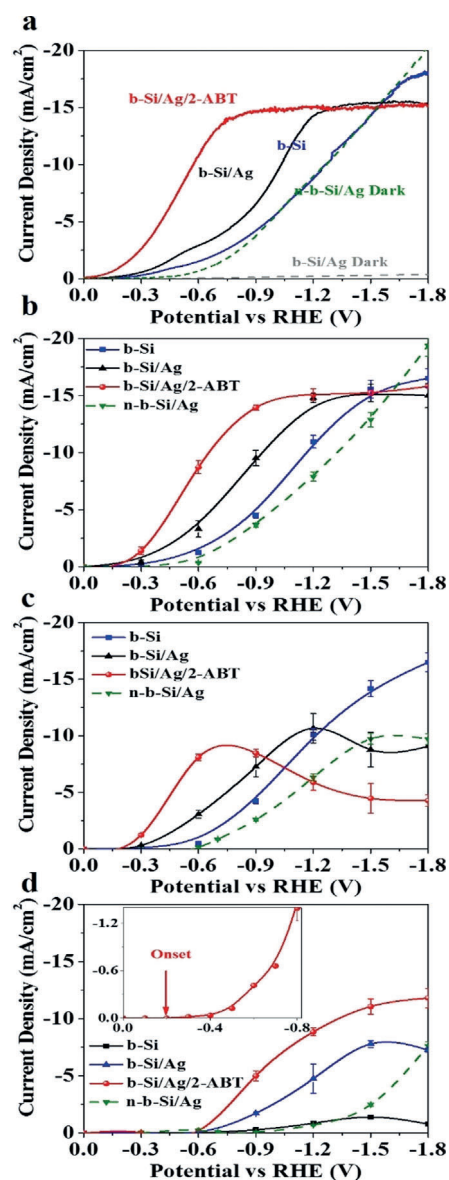


Figure 6. a) LSVs of b-Si, b-Si/Ag, b-Si/Ag/2-ABT measured at scan rate of 50 mVs^{-1} without stirring in 0.2 M KHCO_3 saturated with CO_2 under illumination at approximately 66 mWcm^{-2} with an AM 1.5 filtered spectrum and 420 nm cutoff filter, together with LSVs of illuminated b-Si/Ag and n-b-Si/Ag in the dark for comparison, b) Simulated LSVs of b-Si, b-Si/Ag, b-Si/Ag/2-ABT (light) and n-b-Si/Ag (dark) calculated from bulk electrolysis data at fixed potentials and with slow stirring, c), d) Partial current densities of b-Si, b-Si/Ag, b-Si/ABT (light) and n-b-Si/ABT (dark) calculated from the Faradaic efficiencies of c) H_2 and d) CO production, as measured by GC. The inset shows an expansion at low overpotential of partial current density for CO_2 reduction at b-Si/Ag/2-ABT.

filter. The limiting current density of b-Si reached 18 mA cm^{-2} , which is comparable to that of previous reports.^[24] The current density of b-Si/Ag was 15.5 mA cm^{-2} which is slightly smaller than that of b-Si (also shown in Figure S14). This loss can be attributed to light absorption by Ag and possibly also to recombination at the Ag/Si interface. Not surprisingly, b-Si/Ag/2-ABT gave essentially the same limiting current density; 2-ABT does not absorb significantly

in the visible or near-IR region of the spectrum (Figure S3) and therefore does not affect light absorption by the b-Si photoelectrode. The current density of b-Si/Ag measured in the dark was negligible as expected. Although the photovoltage shift between b-Si under illumination and n-b-Si in the dark was calculated as 510 mV in Figure S15, the photovoltage shift of b-Si/Ag under illumination and n-b-Si/Ag in the dark was less, indicating a rapid loss of catalytic activity during the course of a LSV measurement. In contrast, under illumination, b-Si/Ag/2-ABT had an onset potential of about -50 mV vs. RHE, around 150 mV more positive than the onset potential for b-Si/Ag, and more than 200 mV positive of the onset for b-Si, which gave a calculated photovoltage shift between b-Si/Ag/2-ABT (light) and n-b-Si/Ag (dark) of 610 mV . This demonstrates that the binding of 2-ABT to the Ag surface significantly accelerates the kinetics of the photocathode.

The limiting current of approximately 15 mA cm^{-2} represents the sum of currents for the H_2 evolution reaction (HER) and the CO_2 reduction reaction (CO_2RR) to CO , both of which are overall two electron (i.e., two photon) processes; the CO_2 reduction current therefore depends on the relative rates of the two reactions, which also determine the Faradaic yield of CO_2 reduction to CO . To further study the competition between HER and CO_2RR , constant voltage photoelectrolysis was carried out in a gas-tight reactor at the relatively slow stirring rate of 200 rpm . Average current densities were calculated for these 1 h tests and the data are plotted in Figure 6b. The order of total electrochemical activities from these data are n-Si/Ag (dark) < b-Si < b-Si/Ag < b-Si/Ag/2-ABT, which is consistent with the instantaneous current densities plotted in Figure 6a. The gaseous products of the bulk electrolysis were collected and quantified by gas chromatography, using pure H_2 and CO for calibration. From these data, partial current densities for HER and CO_2RR were calculated and are plotted as a function of applied potential in Figures 6c,d. The simulated LSVs of HER showed that, under low bias ranging from -0.3 to -0.9 V vs. RHE, the current density of H_2 evolution increases and, in the case of b-Si/Ag/2-ABT, reaches a peak value of around 10 mA cm^{-2} . The onset of hydrogen evolution is more positive at b-Si/Ag/2-ABT than it is for b-Si/Ag or b-Si, indicating that the 2-ABT layer facilitates the transport of H^+ to the catalytic surface. Note that, the onset potential of CO_2RR should be -0.2 V vs. RHE as shown in the inset image in Figure 6d. And under a bias as high as -1.2 V vs. RHE, the current density of b-Si/Ag/2-ABT for HER decreased to 5 mA cm^{-2} , whereas that for CO_2RR increased to 10 mA cm^{-2} . This indicates that H^+ is involved in CO_2 reduction.^[46,50,51] The limiting current of b-Si/Ag/2-ABT for CO_2 reached 11.7 mA cm^{-2} , which is more than 50% higher than that of b-Si/Ag and over 4 times higher than that of b-Si. Further confirmation of stability at a bias of -0.9 V vs. RHE is shown in Figure S16a. The reused (aged) electrodes show both similar photoelectrochemical properties and similar Faradaic efficiencies to freshly prepared electrodes in Figure S16b, indicating that b-Si/Ag/2-ABT is both active and stable for the CO_2RR . The SEM image of b-Si/Ag/2-ABT after the constant voltage test shows no significant change (Figure S4e).

Catalytic mechanism

The photoelectrochemical kinetics of the CO₂RR and HER were further interrogated by changing some components of the system. The catalytic effects of Ag nanoparticles can be understood by comparing data from p-type b-Si and b-Si/Ag photoelectrodes as shown in Figure S14. The porous b-Si electrodes containing only trace Ag from the etching process (Figure 5d) have poor kinetics for CO₂ reduction, as shown in Figure S14b, indicating that the Ag nanoparticles are the active catalyst for CO₂ reduction.^[52] As a supporting light absorber, the porous architecture of the b-Si electrode can have several effects. The higher surface area of b-Si affects the catalytic surface area, the recombination rate and the dark current density. The improved light absorbing and catalyst loading properties of b-Si relative to pl-Si are evident in Figures S14a and S14c, as already reported in our previous studies.^[41,53] The porous structure can affect the transport of protons, resulting in higher Faradaic efficiency for the CO₂RR, as reported by Hall, et al. with porous gold electrodes.^[54] In order to evaluate the relative importance of photoelectrocatalysis inside the pores of b-Si/Ag, we polished the top surface of Ag-loaded b-Si with polyimide tape, paper

and water/acetone solution in turn to remove Ag nanoparticles from the top surface. The limiting current density of CO at these polished b-Si/Ag was about 75 % of that obtained without polishing (Figure S12d), suggesting that Ag nanoparticles within the pores are the primarily site of photoelectrocatalysis in b-Si/Ag, and that there is relatively little effect of the pore structure on proton transport at photoelectrochemical current densities.

The most intriguing effect we observe is the acceleration of both the CO₂RR and HER by adsorption of 2-ABT (Figure 7). To gain a better understanding of this effect, we carried out control experiments by using aniline (AP), thiophenol (TP) and 4-ABT, which is the *para* isomer of 2-ABT, as electrode modifiers. Although adsorption of all four molecules lowered the photocurrent onset potential relative to unmodified b-Si/Ag, only AP gave a comparable onset potential to 2-ABT (Figure 7b-f). While these molecules could be bound to the Ag surface through either their -NH₂ or -SH groups, it is interesting to note that 4-ABT and TP have comparable effects to each other and much less effect than 2-ABT or AP. This suggests that surface coordination through thiol groups is controls the orientation of the 4-ABT, 2-ABT, and TP molecules, and that the proximity of the amino group

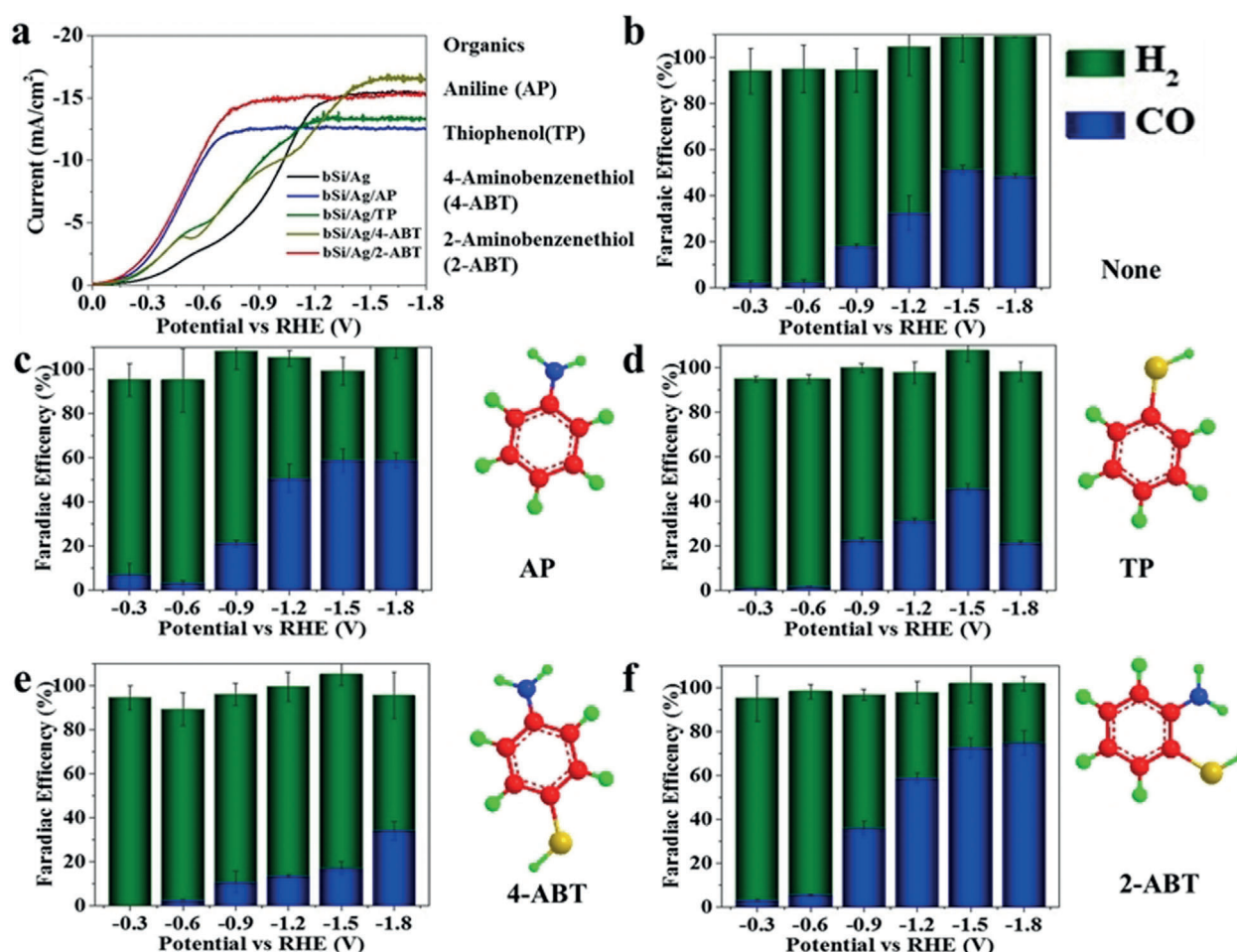


Figure 7. a) LSVs of b-Si/Ag, b-Si/Ag/AP, b-Si/Ag/TP, b-Si/Ag/4-ABT, and b-Si/Ag/2-ABT, column graph of Faradaic efficiency with b) no modification, c) aniline (AP), d) thiophenol (TP), e) 4-aminobenzenethiol (4-ABT) and f) 2-aminobenzenethiol (2-ABT) for CO₂RR and HER, calculated from bulk electrolysis GC data at each potential. Relevant molecular structures are shown at the right in each case.



to the electrode surface (2-ABT and AP) is important in photoelectrocatalysis of the CO₂RR and HER.^[11] The comparable behavior of 4-ABT and TP is consistent with this hypothesis: thiol coordination of Ag positions the NH₂ group of 4-ABT away from the electrode surface, and TP lacks an amino group. On the other hand, the *ortho* arrangement of thiol and amino groups in 2-ABT positions the NH₂ group near the surface. The exact role of the NH₂ group in electrocatalysis is unclear. It could potentially mediate proton transfer, or bind CO₂ as a carbamate intermediate. The fact that adsorption of either 2-ABT or AP accelerates both the HER (as well as the CO₂RR) suggests that mediation of proton transfer is important, as it is in other CO₂RR catalyst schemes that position amines near a catalytic metal center. In order to test the generality of the effect of primary amine electrode modifiers, we also experimented with N₂H₄ treatment, which initially gave an anodic shift in photocurrent onset similar to that of 2-ABT, Figure S17. Presumably in this case the hydrazine molecule is anchored to the Ag surface by one or both -NH₂ groups. However, the effect is transient, possibly because the molecule desorbs or decomposes after the first scan.

To gain insight into the bonding of thiol and amino groups to the Ag surface, water contact angles were measured on p-Si/Ag with the four different electrode modifiers, and the data are shown in Figure S18. HF-treated p-Si was hydrophobic, as expected from Si-H surface termination. Modification by Ag nanoparticles made the surface more hydrophilic and adsorption of the four electrode modifiers had relatively small effects, with all contact angles in the range of 50–60°. From this we can conclude that the different effects of the four electrode modifiers were not a consequence of the ability of water to penetrate the pores of b-Si, that is, hydrophilicity is not the decisive factor in this experiment.

To test the hypothesis that 2-ABT interacts with CO₂ through covalent (e.g., carbamate) or noncovalent interactions, Ag NPs with diameters ranging from 500 nm to 1 μm were modified with 2-ABT and the adsorption of CO₂ was measured at room temperature and low pressure. With the BET surface area calibrated with N₂ adsorption, the amount of CO₂ adsorbed on Ag/2-ABT nanoparticles is much higher than that on unmodified Ag nanoparticles, as shown in Figure S19. Although the saturation values ($q_m \approx 1.5 \times 10^{-9} \text{ mol cm}^{-2}$) are roughly same for both Ag/TP and Ag/2-ABT, CO₂ has a stronger affinity for the 2-ABT modified surface, resulting 10 times higher capacity than bare Ag at 1 atm CO₂ pressure.

Conclusion

This study demonstrates that porous p-type b-Si/Ag is an effective photoelectrode for the reduction of CO₂ to CO. Interestingly, the adsorption of ultrathin 2-ABT accelerates both the CO₂RR and HER at the catalytic Ag surface. Based on control experiments carried out with structurally related aromatic amines and thiols, we can tentatively conclude that the molecule binds the Ag surface through its thiol group and the amino group in the *ortho* position plays a role in

facilitating transport of CO₂ and protons to the metal surface. Further studies are needed to understand the structure of surface-adsorbed 2-ABT and the mechanistic details of the photoelectrochemical reduction of CO₂.

Acknowledgements

Research at the University of Pennsylvania was supported by the Office of Basic Energy Sciences, Division of Chemical Sciences, Geosciences, and Energy Biosciences, Department of Energy, under contract DE-SC0019781. The work performed at Shanghai Jiao Tong University was supported by the NSFC (21777096). M.K. gratefully acknowledges financial support from the China Scholarship Council.

Conflict of interest

The authors declare no conflict of interest.

Keywords: 2-aminobenzenethiol · CO₂ reduction · nanoporous materials · Si photocathodes · silver nanoparticles

- [1] J. M. Matter, M. Sture, S. Ó. Snæbjörnsdóttir, E. H. Oelkers, S. R. Gislason, E. S. Aradóttir, B. Sigfusson, I. Gunnarsson, H. Sigurdardóttir, E. Gunnlaugsson, G. Axelsson, H. A. Alfredsson, D. Wolff-Boenisch, K. Mesfin, D. F. de la Reguera Taya, J. Hall, K. Dideriksen, W. S. Broecker, *Science* **2016**, 352, 1312–1314.
- [2] A. Malik, J. Lan, M. Lenzen, *Environ. Sci. Technol.* **2016**, 50, 4722–4730.
- [3] C. Liu, B. C. Colon, M. Ziesack, P. A. Silver, D. G. Nocera, *Science* **2016**, 352, 1210–1213.
- [4] C. W. Li, J. Ciston, M. W. Kanan, *Nature* **2014**, 508, 504–507.
- [5] W. H. Wang, Y. Himeda, J. T. Muckerman, G. F. Manbeck, E. Fujita, *Chem. Rev.* **2015**, 115, 12936–12973.
- [6] C. Costentin, M. Robert, J. M. Saveant, *Chem. Soc. Rev.* **2013**, 42, 2423–2436.
- [7] R. Francke, B. Schille, M. Roemelt, *Chem. Rev.* **2018**, 118, 4631–4701.
- [8] Y. Ye, H. Yang, J. Qian, H. Su, K. J. Lee, T. Cheng, H. Xiao, J. Yano, W. A. Goddard 3rd, E. J. Crumlin, *Nat. Commun.* **2019**, 10, 1875.
- [9] S. X. Bai, Q. Shao, P. T. Wang, Q. G. Dai, X. Y. Wang, X. Q. Huang, *J. Am. Chem. Soc.* **2017**, 139, 6827–6830.
- [10] C. Kim, H. S. Jeon, T. Eom, M. S. Jee, H. Kim, C. M. Friend, B. K. Min, Y. J. Hwang, *J. Am. Chem. Soc.* **2015**, 137, 13844–13850.
- [11] Z. Han, R. Kortlever, H.-Y. Chen, J. C. Peters, T. Agapie, *ACS Cent. Sci.* **2017**, 3, 853–859.
- [12] M. B. Ross, P. De Luna, Y. Li, C.-T. Dinh, D. Kim, P. Yang, E. H. Sargent, *Nat. Catal.* **2019**, 2, 648–658.
- [13] B. A. Rosen, A. Salehi-Khojin, M. R. Thorson, W. Zhu, D. T. Whipple, P. J. A. Kenis, R. I. Masel, *Science* **2011**, 334, 643–644.
- [14] S. B. Liu, H. B. Tao, L. Zeng, Q. Liu, Z. G. Xu, Q. X. Liu, J. L. Luo, *J. Am. Chem. Soc.* **2017**, 139, 2160–2163.
- [15] M. D. Porosoff, B. H. Yan, J. G. G. Chen, *Energy Environ. Sci.* **2016**, 9, 62–73.
- [16] B. A. Parkinson, P. F. Weaver, *Nature* **1984**, 309, 148–149.



- [17] J. L. White, M. F. Baruch, J. E. Pander, Y. Hu, I. C. Fortmeyer, J. E. Park, T. Zhang, K. Liao, J. Gu, Y. Yan, T. W. Shaw, E. Abelev, A. B. Bocarsly, *Chem. Rev.* **2015**, *115*, 12888–12935.
- [18] M. Halmann, *Nature* **1978**, *275*, 115.
- [19] T. Inoue, A. Fujishima, S. Konishi, K. Honda, *Nature* **1979**, *277*, 637–638.
- [20] Y. J. Jang, J. W. Jang, J. Lee, J. H. Kim, H. Kumagai, J. Lee, T. Minegishi, J. Kubota, K. Domen, J. S. Lee, *Energy Environ. Sci.* **2015**, *8*, 3597–3604.
- [21] M. F. Kuehnel, K. L. Orchard, K. E. Dalle, E. Reisner, *J. Am. Chem. Soc.* **2017**, *139*, 7217–7223.
- [22] E. E. Barton, D. M. Rampulla, A. B. Bocarsly, *J. Am. Chem. Soc.* **2008**, *130*, 6342–6344.
- [23] Y. Hou, B. L. Abrams, P. C. Vesborg, M. E. Björketun, K. Herbst, L. Bech, A. M. Setti, C. D. Damsgaard, T. Pedersen, O. Hansen, *Nat. Mater.* **2011**, *10*, 434.
- [24] J. Oh, T. G. Deutsch, H. Yuan, H. M. Branz, *Energy Environ. Sci.* **2011**, *4*, 1690–1694.
- [25] H. Savin, P. Repo, G. Von Gastrow, P. Ortega, E. Calle, M. Garín, R. Alcubilla, *Nat. Nanotechnol.* **2015**, *10*, 624.
- [26] M. Azuma, K. Hashimoto, M. Hiroamoto, M. Wantanabe, T. Sakata, *J. Electrochem. Soc.* **1990**, *137*, 1772–1778.
- [27] K. Hirota, D. A. Tryk, T. Yamamoto, K. Hashimoto, M. Okawa, A. Fujishima, *J. Phys. Chem. B* **1998**, *102*, 9834–9843.
- [28] K. D. Yang, Y. Ha, U. Sim, J. An, C. W. Lee, K. Jin, Y. Kim, J. Park, J. S. Hong, J. H. Lee, H.-E. Lee, H.-Y. Jeong, H. Kim, K. T. Nam, *Adv. Funct. Mater.* **2016**, *26*, 233–242.
- [29] C. Rogers, W. S. Perkins, G. Veber, T. E. Williams, R. R. Cloke, F. R. Fischer, *J. Am. Chem. Soc.* **2017**, *139*, 4052–4061.
- [30] K. R. Rao, S. Pishgar, J. Strain, B. Kumar, V. Atla, S. Kumari, J. M. Spurgeon, *J. Mater. Chem. A* **2018**, *6*, 1736–1742.
- [31] Y. Kim, E. B. Creel, E. R. Corson, B. D. McCloskey, J. J. Urban, R. Kostecki, *Adv. Energy Mater.* **2018**, *8*, 1800363.
- [32] J. T. Song, H. Ryoo, M. Cho, J. Kim, J. G. Kim, S. Y. Chung, J. Oh, *Adv. Energy Mater.* **2017**, *7*, 1601103.
- [33] X. Yu, V. De Waele, A. Lofberg, V. Ordonsky, A. Y. Khodakov, *Nat. Commun.* **2019**, *10*, 700.
- [34] S. K. Choi, U. Kang, S. Lee, D. J. Ham, S. M. Ji, H. Park, *Adv. Energy Mater.* **2014**, *4*, 1301614.
- [35] W. C. Sheng, S. Kattel, S. Y. Yao, B. H. Yan, Z. X. Liang, C. J. Hawxhurst, Q. Y. Wu, J. G. G. Chen, *Energy Environ. Sci.* **2017**, *10*, 1180–1185.
- [36] F. Urbain, P. Tang, N. M. Carretero, T. Andreu, L. G. Gerling, C. Voz, J. Arbiol, J. R. Morante, *Energy Environ. Sci.* **2017**, *10*, 2256–2266.
- [37] E. Olszewski, M. Albinak, *J. Inorg. Nucl. Chem.* **1965**, *27*, 1431–1433.
- [38] S. Hus, M. Kolar, P. Krajnc, *J. Chromatogr. A* **2016**, *1437*, 168–175.
- [39] A. R. Morales, G. Luchita, C. O. Yanez, M. V. Bondar, O. V. Przhonska, K. D. Belfield, *Org. Biomol. Chem.* **2010**, *8*, 2600–2608.
- [40] L. G. AbdulHalim, N. Kothalawala, L. Sinatra, A. Dass, O. M. Bakr, *J. Am. Chem. Soc.* **2014**, *136*, 15865–15868.
- [41] Y. Zhao, N. C. Anderson, K. Zhu, J. A. Aguiar, J. A. Seabold, J. van de Lagemaat, H. Branz, N. Neale, J. Oh, *Nano Lett.* **2015**, *15*, 2517–2525.
- [42] Z. Huang, N. Geyer, P. Werner, J. de Boor, U. Gosele, *Adv. Mater.* **2011**, *23*, 285–308.
- [43] Z. Wang, A. Bonoiu, M. Samoc, Y. Cui, P. N. Prasad, *Biosens. Bioelectron.* **2008**, *23*, 886–891.
- [44] Y. Wang, X. Zou, W. Ren, W. Wang, E. Wang, *J. Phys. Chem. B* **2007**, *111*, 3259–3265.
- [45] G. Xue, M. Ma, J. Zhang, Y. Lu, *J. Colloid Interface Sci.* **1992**, *150*, 1–6.
- [46] J. Rosen, G. S. Hutchings, Q. Lu, S. Rivera, Y. Zhou, D. G. Vlachos, F. Jiao, *ACS Catal.* **2015**, *5*, 4293–4299.
- [47] Q. Lu, J. Rosen, Y. Zhou, G. S. Hutchings, Y. C. Kimmel, J. G. G. Chen, F. Jiao, *Nat. Commun.* **2014**, *5*, 3242.
- [48] F. S. Legge, G. L. Nyberg, J. B. Peel, *J. Phys. Chem. A* **2001**, *105*, 7905–7916.
- [49] I. Nakai, Y. Matsumoto, N. Takagi, S. Okazaki, *J. Chem. Phys.* **2008**, *129*, 154709.
- [50] C. Costentin, S. Drouet, M. Robert, J. M. Saveant, *Science* **2012**, *338*, 90–94.
- [51] M. R. Singh, J. D. Goodpaster, A. Z. Weber, M. Head-Gordon, A. T. Bell, *Proc. Natl. Acad. Sci. USA* **2017**, *114*, E8812–E8821.
- [52] J. W. Beeman, J. Bullock, H. Wang, J. Eichhorn, C. Towle, A. Javey, F. M. Toma, N. Mathews, J. W. Ager, *Energy Environ. Sci.* **2019**, *12*, 1068–1077.
- [53] M. Kan, J. Jia, Y. Zhao, *RSC Adv.* **2016**, *6*, 15610–15614.
- [54] A. S. Hall, Y. Yoon, A. Wuttig, Y. Surendranath, *J. Am. Chem. Soc.* **2015**, *137*, 14834–14837.

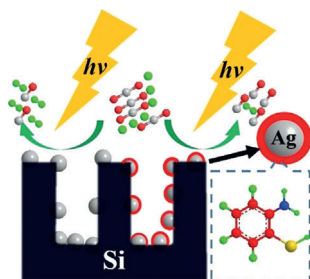
Manuscript received: February 6, 2020
Accepted manuscript online: April 5, 2020
Version of record online: ■ ■ ■ ■ ■ ■ ■ ■ ■ ■

Research Articles

CO₂ Reduction

M. Kan, Z. F. W. Yan, X. T. Wang, J. L. Hitt,
L. Q. Xiao, J. M. McNeill, Y. Wang,
Y. X. Zhao,*
T. E. Mallouk* ————— ■■■■-■■■■

2-Aminobenzenethiol-Functionalized
Silver-Decorated Nanoporous Silicon
Photoelectrodes for Selective CO₂
Reduction



Silver lining: The adsorption of 2-amino-benzenethiol (2-ABT) onto nanoporous p-type black silicon (b-Si) photocathodes decorated with Ag nanoparticle catalysts lowers the overpotential and improves the selectivity of CO₂ reduction to CO.

